Highlights

- Localized heating of feed water using inbuilt heating element in MD is proposed.
- Novel dead-end MD-intermittent flush system is most efficient.
- 133% increase in water vapor production is achieved.
- GOR increased by 132% and SEC decreased by 57%.
- SEC of new concept approaches theoretical thermodynamic limit for water evaporation.

Dead-end membrane distillation with localized interfacial heating for sustainable and energy-efficient desalination

Mustakeem Mustakeem, Adnan Qamar, Alla Alpatova, Noreddine Ghaffour *

King Abdullah University of Science and Technology (KAUST), Water Desalination and Reuse Center (WDRC), Biological and Environmental Science and Engineering Division (BESE), Thuwal 23955-6900, Saudi Arabia

* Corresponding author, Email: noreddine.ghaffour@kaust.edu.sa

Abstract

Membrane distillation (MD) has the high potential to circumvent conventional desalination limitations in treating highly saline brines. However, the performance of MD is limited by its low thermal efficiency and temperature polarization (TP) effect. Consequently, the driving force decreases when heat loss increases. In this study, we propose to minimize TP through localized heating where the thin feed channel was heated uniformly at the membrane-liquid interface without changing the properties of the membrane. This concept was further improved by implementing a new dead-end MD configuration. Investigated for the first time, this configuration eliminated circulation heat losses, which cannot be realized in conventional MD due to a rapid temperature stratification. In addition, the accumulation of foulants on the membrane surface was successfully controlled by intermittent flushing. 3-Dimensional conjugate heat transfer modeling revealed more uniform heat transfer and temperature gradient across the membrane due to the increased feed water temperature over a larger membrane area. The increase of water vapor flux (45%) and the reduction of heat loss observed in the new

dead-end concept led to a decrease of the specific energy consumption by 57%, corresponding to a gain output ratio increase of about 132 %, compared to a conventional bulk heating, while preserving membrane integrity. A conjugate heat transfer model was deployed in ANSYS-Fluent framework to elucidate on the mechanism of flux enhancement associated with the proposed technique. This study provides a framework for future sustainable MD development by maintaining a stable vapor flux while minimizing energy consumption.

Keywords: Membrane distillation (MD), desalination, localized heating, temperature polarization, dead-end, heating element.

Nomenclature		**Units**	**Greek symbols**	
ı	Membrane permeability	Kg/(m^2·s·Pa)	λ	Mean free path
,	Specific heat capacity of water	kJ/kg·K	χ	Membrane tortuosity
	Pore diameter	m	ε	Membrane porosity
	Diffusion coefficient	m^2/s	δ	Membrane thickness
	Total Energy	Joule	$\bar{\bar{\tau}}$	Stress tensor
ı	Electric energy input	kWh	σ	Collision diameter of water vapor molecule
g	Latent heat of vaporization	kJ/kg	**Subscripts**	
	Flux	Kg/m^2·s	v	Water vapors
	Molecular weight of water	Kg/mol	m	Membrane
	Mass flow rate	Kg/s	p	Permeate
	Vapor pressure	Pa	i	Inlet

ι	Air pressure	Pa	f	Feed	
	Ideal gas constant	J/mol·K		**Acronyms**	
	Temperature	K	BH	Conventional bulk heating	
	Time	s	$LHCF$	Localized heating-cross flow	
ι	Knudsen number	NA	$LHDE$	Localized heating-dead-end	
ȝ	Boltzmann constant	J/K	$LHIF$	Localized heating-dead-end-intermittent flush	

1. Introduction

Water desalination has manifested itself as a sustainable and reliable means of freshwater production, not only in arid and semi-arid regions of the Middle East and Northern Africa (MENA), but also in coastal countries with moderate weather conditions (Caldera and Breyer, 2017; Ghaffour et al., 2013). Consequently, the water desalination industry has grown exponentially in recent decades currently employing more than 18,000 desalination plants around the world (IDA, 2015; Jones et al., 2019). Membrane distillation (MD) is an emerging desalination process which can produce high quality water from both natural water sources like seawater (Andrés-Mañas et al., 2018; Shim et al., 2015) or groundwater (Naji et al., 2020; Plattner et al., 2017) as well as from brines (Elcik et al., 2020; Sanmartino et al., 2017; Schwantes et al., 2018). Its moderate operating conditions make it a promising economical and energy-saving desalination approach (Alsaadi et al., 2015; Curcio and Drioli, 2005; Subramani and Jacangelo, 2015; Yang et al., 2014). Contrary to seawater reverse osmosis (SWRO), MD does not require high-grade electrical energy for its operation, and works in a lower feed water temperature range compared to multi-stage flush (MSF) while producing high quality

freshwater. MD also has an advantage in treating highly saline feed waters, facilitating high salt rejection and low fouling propensity as compared to other well-established desalination technologies (Kim et al., 2016; Subramani and Jacangelo, 2015; Wang, 2018; Wang and Chung, 2015). However, despite the high potential of the MD process to circumvent conventional desalination technologies, its energy consumption remains ambiguous due to inherent heat loss by conduction and evaporation (Eleiwi et al., 2016; Summers et al., 2012; Yang et al., 2014).

In the conventional MD system, the bulk feed water is heated externally, causing up to 50% of the conduction heat loss due to the heat released in the atmosphere (Fane et al., 1987; Lokare et al., 2018)). Furthermore, when the feed water enters the MD module, its bulk temperature is higher compared to the membrane surface because of convective energy losses and latent heat release during the liquid to gas phase transition (Elmarghany et al., 2019; Lee et al., 2016). The extent to which feed temperature at the membrane surface differs from its bulk value is known as temperature polarization (TP). TP can be as high as 10 °C, leading to decreased heat and mass transport rates across the membrane (Alsaadi et al., 2018; Rezaei et al., 2018). Consequently, the MD energy efficiency decreases due to the limitations of the thermal boundary layer at the membrane-liquid interface (Alsaadi et al., 2018; Santoro et al., 2017). Several studies have mitigated TP by using turbulence creators such as spacers; however, this approach creates additional pressure on energy requirements (Kim et al., 2018; L Martinez and Diaz, 1998; Seo et al., 2017; Shakaib et al., 2012; Taamneh and Bataineh, 2017). Taking into consideration that TP and conduction heat loss is an inherent process deficiency which cannot be fully mitigated, it is highly desirable to seek alternative approaches to alleviate heat loss and achieve a sustainable MD performance.

A recently developed approach, called localized heating, supplies the heat energy directly to the membrane-liquid interface, maintaining a stable temperature regime across the membrane. As a result, the evaporation process can be augmented at the membrane's surface. The concept of localized heating can be realized through the self-heating membranes. Some researchers have attempted to develop these membranes using photo-thermal materials which can convert light energy into heat, using the thermo-plasmonic effect (Dongare et al., 2017; Politano et al., 2017; Tan et al., 2018; Wu et al., 2018; Ye et al., 2019). The Joule heating phenomenon, in which the kinetic energy of electrons is converted into thermal energy upon passing electrical currents (Anvari et al., 2019; Boo and Elimelech, 2017; Dudchenko et al., 2017; Song et al., 2019), is another example of supplying energy to a membrane surface. Dudchenko et al. investigated localized heating in MD, using Joule heating on a carbon nanotube composite MD membrane (Dudchenko et al., 2017). Shukla et al. also studied the concept of localized heating of a hollow fiber membrane in sweeping gas MD (Shukla et al., 2015). In a more recent approach, Anvari et al. demonstrated localized heating with radio frequency-based induction coupling, where energy was transferred remotely through an induction heating power supply (Anvari et al., 2019). The concept of self-heating membranes has been well-explored in the context of localized heating and has obtained improved flux results (Jiang et al., 2019); however, all such approaches are based on manipulating the membrane surface properties. The membrane surface properties (such as wettability and adhesiveness) are crucial in ensuring the membrane functionality in MD. In addition, the stability of coating material may degrade, leading to a decrease in water flux and overall system performance, especially for larger scale applications. To push MD technology into new energy-efficient realms, a viable solution to confront TP, while maintaining membrane

integrity, needs to be found. To the best of our knowledge, no studies have been demonstrated to conceptualize localized heating that does not affect the membrane surface properties.

In our study, we propose to provide the heat energy locally, inside the membrane module, close to the feed membrane-liquid interface using an electric heating coil. By delivering the heat locally, a stable temperature regime can be maintained without manipulating the membrane. As the heating coil only heats a thin layer of the feed water at the membrane–liquid interface, the TP effect will decrease; hence the water vapor flux will increase, leading to a decrease in the specific energy consumption (improved gain output ratio, GOR) compared to the conventional bulk feed water heating.

Additionally, a new dead-end DCMD configuration (zero feed circulation) combined with localized heating was investigated and reported for the first time. This showed the elimination of circulation heat loss, which cannot be realized in conventional MD due to rapid temperature stratification. The system's overall performance significantly improved, with the energy efficacy approaching the thermodynamic minimum energy requirement for water evaporation. Three-dimensional (3-D) numerical calculations were simultaneously performed for each tested MD configuration, to elucidate the heat transfer mechanism and associated permeate flux enhancement. We embedded a nichrome heating coil in a circular shaped MD flow cell setup and performed experiments on different MD configurations in order to compare the performance parameters between the conventional bulk heating and the localized heating.

2. Materials and methods

2.1. Feed and coolant waters

Red Sea water (conductivity: 58.8 mS/cm, see detailed composition in Table S4, supplementary material) without any pretreatment was used as feed water and RO water (conductivity: 0.015 mS/cm) was used as permeate/coolant water in all experiments.

2.2. Heating coil

Although we aspired to have a spacer-shaped heating element, it is challenging to fabricate such elements and achieve a stable performance in highly saline environments (e.g., seawater). Thus, to gauge the localized heating concept, and for simplicity, a commercial heating coil (nichrome wire) was utilized, as shown in Fig. 1A. Such a coil is expected to be stable under the highly ionic environments because the Nichrome wire inside the coil is protected by the electrical insulation.

2.3. Heating configurations

Three different configurations were tested using a large membrane surface area, as shown in Fig. 1: (B) conventional DCMD process with bulk heating (BH), (C) localized heating cross-flow (LHCF), in which the heating is applied only inside the feed channel and feed is circulating in the same manner as in conventional DCMD, and (D) localized heating dead-end (LHDE) with no feed circulation and localized heating dead-end with intermittent feed channel flush (LHIF).

2.3.1. Bulk-heating configuration

Fig. 1B presents a schematic diagram of the bulk-heating configuration. The DCMD process was conducted in a counter-current mode, and the feed and coolant were supplied to the module from the corresponding feed and coolant tanks by using gear pumps (Model 75211, Cole-Parmer, USA) with flow rates of 300 mL/min and 280 mL/min, respectively. The feed flow rate was set to 20 mL/min more than the permeate flow to compensate the flow effect of pump gear assembly at an elevated temperature. The cooling and heating were achieved by circulation bathes (Model 600-F, Julabo, Germany). The feed and coolant temperatures were set at 60°C and 25°C, respectively. The inlet and outlet temperatures of feed and coolant were measured by the 10K thermistors and recorded by a multiplexer data logger (Model 34972A, Keysight, USA). An additional 10K thermistor was used as a feedback control to maintain a stable feed water temperature of 60°C. The mass of coolant was recorded by a digital balance (Model ML6002T, Mettler Toledo, USA).

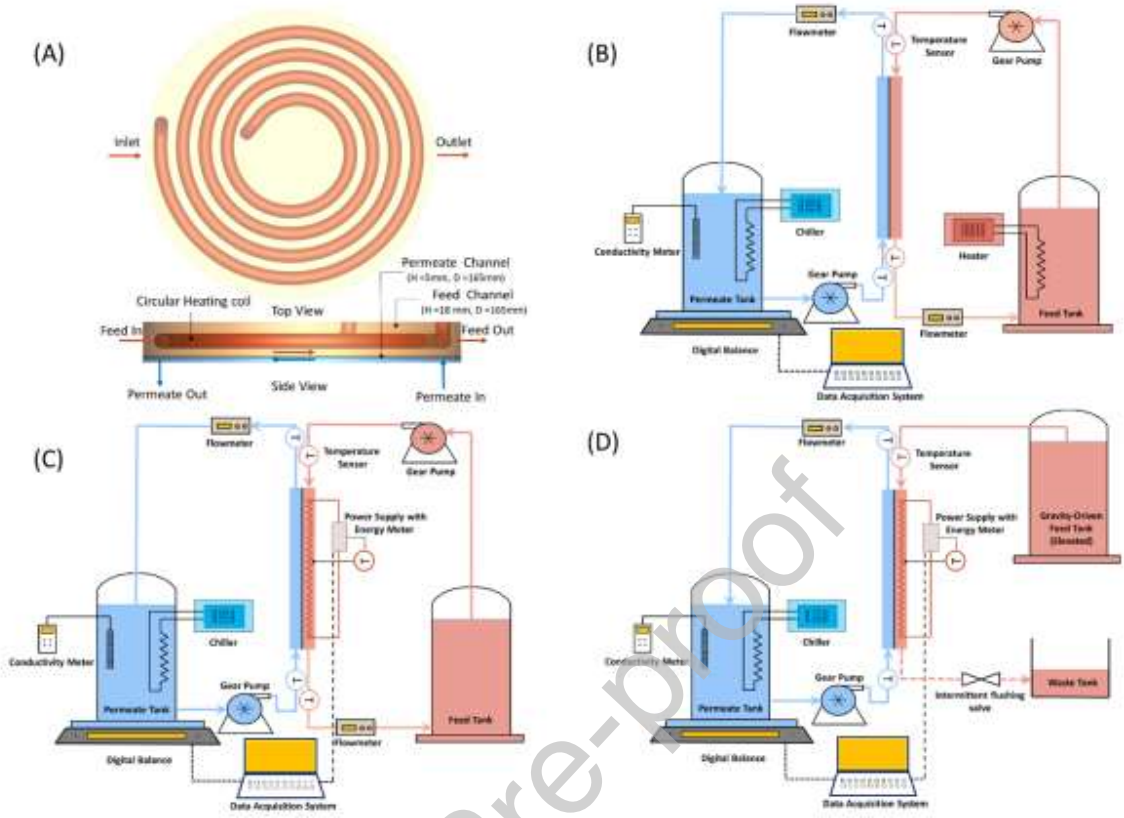

Fig. 1. (A) Schematic of circular DCMD module fabricated in-house with a commercially available heating element, (B) Conventional bulk heating (BH) DCMD set up, (C) Localized heating cross-flow (LHCF), and (D) Localized heating dead-end (LHDE) and localized heating dead-end with intermittent flush (LHIF), feeding the feed channel from an elevated feed tank without feed recirculation.

2.3.2. Localized heating MD module with an embedded heating element

An acrylic MD module with the active membrane area of 0.0213 m^2 (165 mm diameter) was fabricated in-house as shown in Figure 1A. The module consisted of two circular channels to accommodate the feed and coolant waters. A heating coil was implanted at the feed side of the module, adjacent to the membrane surface. The associated dimensions of the heating coil and its placement location inside the feed channel are shown in the Supplementary Information (Fig. S1, SI). The temperature inside the module was monitored by the 10K thermistors

(Omega Engineering Inc., UK). A hydrophobic polytetrafluoroethylene (PTFE) membrane (Membrane Solutions, China) with an average pore size of 0.22 μm and 85% porosity (as provided by the manufacturer) was utilized in all experiments.

2.4. Energy and flux calculations

The energy utilization was calculated in two ways: a) energy meter, and b) the first law of thermodynamics using temperature and flow values. Q_{in} (kWh) is the total heat energy supplied to the MD system, calculated from the energy meter reading.

The total heat energy content of the feed water was utilized in three main processes; circulation, conduction and evaporation. The circulation heat Q_{cr} (kW) is the heat dissipated during the feed circulation process, which is the case only in bulk heating. It is calculated from the temperature and flow values by subtracting from the total heat content, Q_{in}:

$$Q_{cr} = Q_{in} - \left(\dot{m}_f * C_p * \Delta T\right) \quad (1)$$

where $\dot{m}_f$ (with an accent mark) is the mass flow rate of feed water (kg/s), C_p is the specific heat energy of water (4.2 kJ/kgK) (Rogers and Y, 2009), and ΔT is the difference between the initial and final feed temperatures.

The heat distribution inside the MD module is comprised of the heat transfer by conduction and evaporation. The heat transfer by evaporation (Q_{ev}, kW) was calculated according to the equation below:

$$Q_{ev} = \dot{m}_d * h_{fg} \quad (2)$$

where $\dot{m}_d$ is the mass flow rate (kg/s) of the water vapor across the membrane, and h_{fg} is the enthalpy of water vaporization (kJ/kg).

The heat transfer by conduction (Q_{cd}, kW) was calculated as follows:

$$Q_{cd} = \left(\dot{m}_f * C_p * \Delta T\right) - Q_{ev} \quad (3)$$

The specific energy consumption (SEC, kWh/m^3) is the energy consumed per 1 m^3 of water production, and was calculated by using the following equation (Jantaporn et al., 2017; Khayet, 2013):

$$SEC = \frac{Q_{in}}{m} \quad (4)$$

where Q_{in} (kWh) is the total electric heat energy supplied to the system, and m is the mass of distillate (kg).

The gain output ratio (GOR) represents the efficiency of a thermal desalination system. It is the ratio of the distillate water produced with the particular energy input (Koschikowski, 2003; Qtaishat and Banat, 2013). It is calculated using the following equation:

$$GOR = \frac{m * h_{fg}}{Q_{in}} \quad (5)$$

The permeate flux J (kg/m^{2}h) was calculated as follows (Song et al., 2019):

$$J = \frac{m}{A * \Delta t} \quad (6)$$

where A is the membrane's active surface area (m^2), and Δt is MD time (h).

2.5. Localized heating configurations

In the localized heating cross-flow configuration (Fig. 1C), the feed water was heated by a build-in heating coil embedded next to a membrane surface. The feed and coolant feed flow rates and temperatures were the same as in the bulk heating configuration. In the localized heating dead-end configuration (Fig. 1D), the feed water was fed by gravity from a feed tank, which was positioned above the MD module and heated by a heating coil inside the MD module. The localized heating dead-end with intermittent flush configuration was similar to

that of the localized heating dead-end, except that the feed water inside the MD module was flushed out to a new portion of feed. The feed pump at a flow rate of 1000 mL/min was used to flush the feed channel for 1 min at 30 minutes interval.

All the MD experiments were conducted based on 1 kWh of the energy input (the same energy consumption), which was recorded by the energy meter (HiSence, China). Each experiment was replicated to ensure its repeatability.

2.6. Analytical and surface characterization techniques

A conductivity meter (Model 3310, WTW, USA) was used to monitor the coolant conductivity to ensure the membrane's integrity during the MD runs. The coolant conductivity was below 15 µS/cm during all experiments.

In order to investigate the heating effect on a surface of polymeric membrane, the membrane was placed inside the MD module and heated locally to 60 ^{o}C using the same feed water. The membranes were extracted and subjected to a range of surface characterization techniques to ensure no surface damage or loss in hydrophobicity occurred after the localized heating process. A scanning electron microscopy, SEM (Zeiss Merlin, Gemini-II, Germany) was employed to observe the changes in membrane morphology. The samples were coated by a 4 nm iridium layer, and SEM imaging was performed at an acceleration voltage of 5 kV. A Fourier transform infrared (FT-IR) spectrometer (Spectrum-100, Perkin Elmer) with an attenuated total reflectance (ATR) attachment in a scanning range of 500 cm^{-1} - 4000 cm^{-1} was utilized to investigate the functional groups present on the membrane surfaces before and after localized heating. The membrane hydrophobicity was determined by measuring surface contact angles using a drop-shape analyzer (Attension Theta, NanoScience, USA).

To ensure that MD module was not damaged upon the coil heating, its surface temperature was measured by using Fluke TiS40 Thermal Infrared camera and no visual signs of module buckling, bending or melting were observed.

2.7. Numerical model

A numerical model was utilized to predict the mass transport through the tested MD configurations. At the pore level, the mass transport through the membrane is primarily determined by the ratio of the mean free path of water vapor molecule to the membrane pore diameter (D_p), referred to as Knudsen number (K_n) (Olatunji and Camacho, 2018):

$$K_n = \frac{\lambda}{D_p} \quad (7)$$

The water vapor mean-free path (λ) can be determined as (Olatunji and Camacho, 2018):

$$\lambda = \frac{k_B T_m}{\sqrt{2} P_m \sigma_v^2} \quad (8)$$

where k_B is the Boltzmann constant ($1.38 \cdot 10^{-23}$ J/K), P_m is the mean average pressure in membrane pores (Pa), T_m is the membrane surface temperature, and σ is the water vapor collision diameter (0.2641 nm).

Depending on the value of K_n, three possible mass transfer modes exist as follows: (a) Knudsen diffusion ($K_n > 1$) in which molecular collisions with the walls dominate as compared to the gas-gas collisions, (b) molecular diffusion ($K_n < 0.01$) in which the frequency of gas molecule collisions is much higher than those with the pore walls, and (c) Knudsen-molecular diffusion ($0.01 < K_n < 1$) in which the frequency of molecular collisions with the pore walls is similar to that of the gas-gas collisions (often referred to as "transitional regime") (Olatunji and Camacho, 2018). Based on the membrane pore diameter, the Knudsen number was calculated to be $K_n \approx 0.5$. It implies that for the membrane used in the experiments, the mass transport

mode is primarily determined by the Knudsen-molecular diffusion theory (Olatunji and Camacho, 2018).

According to the Knudsen-molecular diffusion theory, the flux of an ideal gas through a pore is directly proportional to that of the pressure difference according to the following equation:

$$J = C_m * \left(P_{m,f} - P_{m,p}\right) \tag{9}$$

where C_m is the mass transfer coefficient ($Lm^{-2}s^{-1}Pa^{-1}$), $P_{m,f}$ and $P_{m,p}$ are the vapor pressures (Pa) of the feed and permeate on the membrane surface, respectively. The vapor pressure P_v (Pa) was calculated using Antoine's equation (Olatunji and Camacho, 2018), for a given membrane surface temperature T_m (K) as:

$$P_v = Exp\left[23.19 - \left(\frac{3816.44}{T_m - 46.13}\right)\right] \tag{10}$$

The mass transfer coefficient, C_m, was determined according to the kinetic theory (Olatunji and Camacho, 2018):

$$C_m = \left[\left\{\frac{\varepsilon D_p}{3\delta\chi}\sqrt{\frac{8M}{\Pi RT}}\right\}^{-1} + \left\{\frac{\varepsilon}{\chi\delta}\frac{DM}{RT}\frac{P_T}{P_a}\right\}^{-1}\right]^{-1} \tag{11}$$

where M, χ, ε, D_p, δ, D, P_T, P_a, R and T are the molecular weight of the water molecule (kg/mole), membrane tortuosity, membrane porosity, pore radius (m), membrane thickness (m), water-air diffusion coefficient, average air pressure (Pa), total pressure (Pa), ideal gas constant (J/mole·K), and mean temperature (K), respectively.

In order to predict membrane surface temperatures (T_m) on the feed and permeate sides, a conjugate heat transfer calculation coupled with the Navier-Stokes equation was performed on the exact replicate of the MD module and configurations which were used in this study (see Section S1, SI for computational domain used and mesh independence). The numerical details,

including appropriate governing equations and relevant boundary conditions, are presented elsewhere (Subramanian et al., 2019). The computations were simultaneously coupled in the fluid domains (feed and permeate channels) with the solid domain (membrane) by appropriate boundary conditions. Present model does not take into account the fouling process and presented modeling results only help to understand the hydrodynamics and the associated physical heat transfer occurring inside the module in different MD configurations. In this model we assumed the feed and permeate to behave like Newtonian fluid with incompressible properties. The governing equations and the parametric values used in the present work are provided in Section S2 (SI).

At each time-step, the conservation equations (3-dimensional mass, momentum and energy equations) were solved using the conjugate heat transfer formulation (ANSYS, 2019). The spatial temperature distribution, flow velocity and pressure distribution were determined on each discretized control volume (total ~30 million) in all computation domains (feed, permeate and membrane). The surface temperature profiles were extracted to compute the vapor pressures as given by the empirical Antoine equation (Eq. (10)). Based on the pressure difference, the permeate flux J (Eq. (9)) at each time was computed using the Knudsen-molecular diffusion theory through a user define function (UDF) in the ANSYS-fluent framework. This procedure was continued until a quasi-steady/steady state was achieved. The whole numerical framework was incorporated in ANSYS-Fluent software (Version 19.0) by employing a second-order space (QUICK(ANSYS, 2019; Qamar et al., 2014)) and time discretization.

The temperature polarization coefficient (TPC) was calculated as below:

$$\tau_{TP} = \frac{T_{FM} - T_{PM}}{T_F - T_P}$$

(12)

where T_{FM} and T_{PM} are the average membrane surface temperatures on the feed and permeate sides, respectively, and T_F (60 °C) and T_P (25 °C) are the bulk feed and permeate temperatures, respectively.

3. Results and discussion

3.1. Improvement of permeate flux by localized heating

Fig. 2 shows permeate fluxes and feed temperatures inside the MD module achieved in different MD configurations as a function of process time at a total energy input of 1 kWh. When the MD system was operated in bulk heating mode (Fig. 2A), it took approximately 50 mins for the feed temperature to reach its set point of 60 ^{o}C. The permeate flux gradually increased until it reached a steady-state value of 5.6 ± 0.3 kg/m^{2}h. The mass of produced permeate in this mode was 362 ± 2 g (Fig. 3).

When the process was run in the localized heating cross-flow mode, a significant improvement in permeate flux was observed (Fig. 2B). In this mode, the feed water was heated only inside the MD module so that the feed temperature reached its set point (60 °C) around 1.7 times faster compared to that of a bulk heating mode. A 10.5% increase in permeate flux was observed once the feed temperature reached its set point (60 ^{o}C) due to diminishing TP upon localized heating. Therefore, the elimination of TP and circulation heat loss leads to longer MD duration per 1 kWh of input energy. Consequently, permeate production increased by almost 80%, reaching 650 ± 22 g (Fig. 3). The localized heating dead-end mode exhibited a significantly better MD performance than the localized heating cross-flow, reaching the set

feed temperature five times faster compared with the bulk heating (Fig. 2C). This was accompanied by an additional 20% increase in the permeate flux, from 6 ± 0.1 kg/m^{2}h to 7.2 ± 1.3 kg/m^{2}h once the feed water temperature reached 60 ^{o}C. Under this condition, a substantially enhanced permeate production of 825 ± 81 g was observed.

However, when the MD system was operated in localized heating cross-flow mode, the permeate flux decreased with the increase in process time (Fig. 2B). This phenomenon was more pronounced in case of localized heating dead-end configuration (Fig. 2C) compared to that of localized heating cross-flow configuration. Although the MD process is the least affected by the feed water salinity as compared to other membrane desalination processes (Curcio and Drioli, 2005; Olatunji and Camacho, 2018; Soukane et al., 2017; Yang et al., 2014), a continuous permeate flux decrease was observed in the localized heating dead-end mode during the entire MD operation due to the accumulation of feed water constituents at the membrane surface. The localized heating dead-end could promote membrane fouling as a result of the rapid development of the concentration boundary layer, which may cause the accumulation of foulants near the membrane surface, hence reducing the mass and heat transfers across the membrane. To address this issue, we introduced an "intermittent flush" configuration (localized heating dead-end with intermittent flush), in which the feed water inside the MD module is flushed at a predetermined time interval of 30 minutes so that the accumulated fouling is washed away from the membrane surface and normal MD operation is resumed. As a result, a maximum permeate flux of 9.8 ± 1.6 kg/m^{2}h (Fig. 2D), corresponding to a mass of produced permeate water per 1 kWh of 845 ± 38 g (Fig. 3), was observed. The application of the intermittent flush allowed a more stable permeate flux which gradually reached its steady state after the fourth flush cycle (Fig. 2D). As a result, the permeate flux at

the end of this process was higher than that achieved with the localized heating dead-end configuration. We therefore expect that the combined effect of localized heating and an intermittent flush will enable a more sustainable MD performance during long-term operations by maintaining a more stable permeate flux while alleviating membrane fouling.

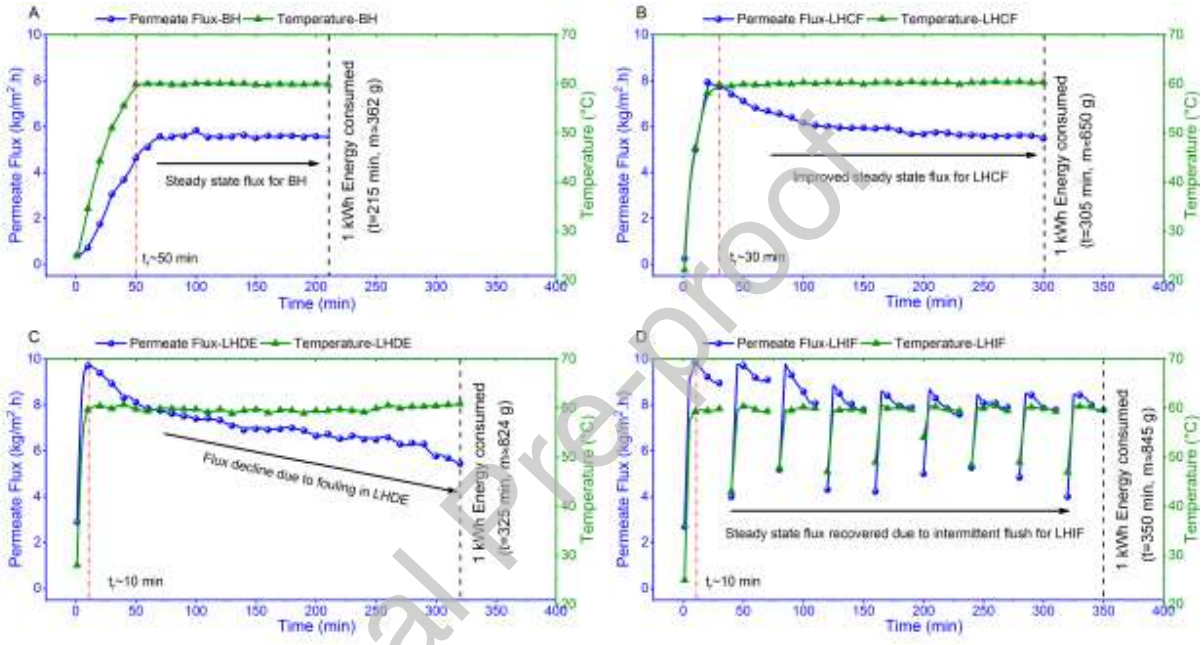

Fig. 2. Permeate flux and temperature profiles of different DCMD configurations: (A) Conventional bulk heating (BH) mode, (B) Localized heating crossflow (LHCF) mode, (C) Localized heating dead-end (LHDE) mode, and (D) Localized heating dead-end with intermittent flush (LHIF) mode. All experiments were run until 1 kWh of energy was consumed. The transient time (t_r) required to achieve a stable feed temperature for each case is also marked along the timeline.

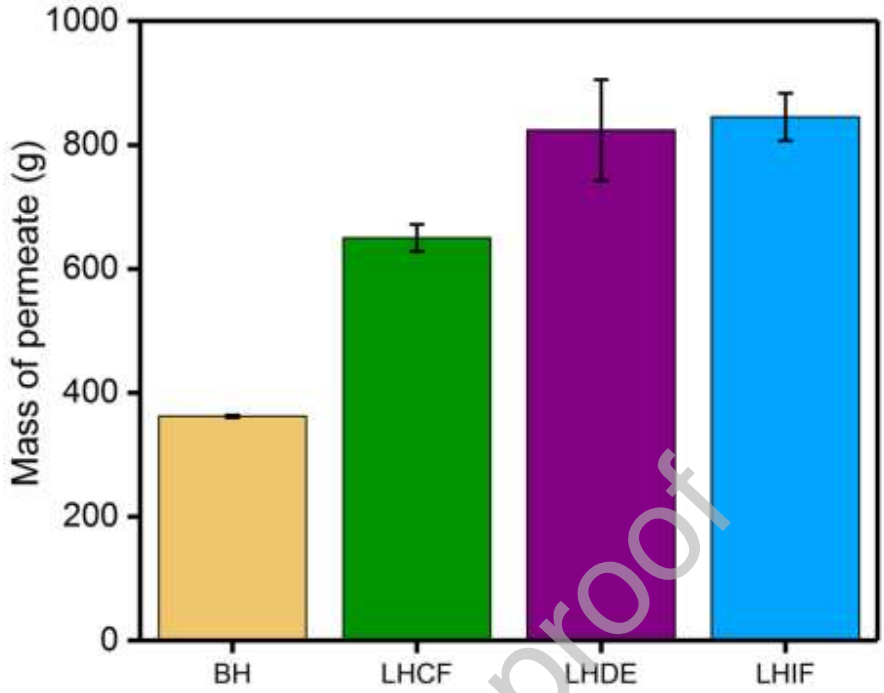

Fig. 3. Mass of permeate water produced per 1 kWh of energy input for different MD configurations. BH: conventional bulk heating mode, LHCF: localized heating cross-flow mode, LHDE: localized heating dead-end mode, and LHIF: localized heating dead-end with intermittent flush mode.

3.2. Heat transfer mechanism and permeate flux enhancement in localized heating

Three-dimensional simulations were conducted to comprehend the physical understanding of the localized heating in various MD configurations and to elucidate the effect of hydrodynamic conditions on the heat transfer process prevailing in each MD configuration. To allow for the comparison of the experimental and modelling results, all flow and geometric conditions as well as membrane properties were assumed similar to those utilized in experimental MD runs. Parametric details of simulations, including model geometry and meshing, are available in the SI. The localized heating dead-end with intermittent flush configuration was not simulated, as flush requires a concentration polarization model to be implemented in numerical framework,

which is beyond the scope of this study. Nevertheless, for the first cycle of a localized heating dead-end with intermittent flush mode, the hydrodynamics and thermal conditions inside the MD module are expected to be the same as for the localized heating dead-end configuration (also evident from experimental flux behavior for the first flush cycle, Fig. 2D). Thus, for the initial physical insight, the results of the localized heating dead-end simulation are sufficient to gauge the localized heating dead-end with intermittent flush performance.

Fig. 4 shows the hydrodynamic conditions (Figs. 4 A-C) and corresponding thermal snapshots that predominated inside the feed channels (Figs. 4 D-E) when the feed temperature inside the feed channel reached its set point of 60 ^{o}C at a location corresponding to a temperature sensor location in the experiments. As seen, the stream traces overlapped with the velocity magnitude, indicating the path and velocity magnitude at various locations when the feed fluid passed through the channel with the heating element installed (Figs. 4 A-C). For the bulk heating and localized heating cross-flow configurations, the feed and permeate flow rates were kept the same as in experimental runs. The only difference was that in the bulk heating mode, the inlet feed water temperature was set to 60 ^{o}C and the heating element was not powered, while in the localized heating mode the feed entered at 24 ^{o}C (ambient temperature), with the powered element to provide thermal heat flux of 14,000 W/m^2 locally near the membrane surface. For these two cases, the hydrodynamics (stream traces and velocity magnitudes) conditions look similar (Fig. 4B). As the feed fluid entered the MD module, it traveled straight until the fluid encountered the central region (the void region with no heating coil filaments). Due to this design of the heating element, two vortices were trapped in the center of the heating coil and divided the whole incoming flow into two sections. As seen in Figs. 4A and B, the recirculating region (marked schematically in Fig. 4A) swept the majority

of the module, with the low velocity having epicenter at the center of the coil. Ahead of this recirculation region, the flow converged and exited out of the MD module. The highest velocity magnitude was observed in the middle region of the MD module. In general, a relatively low velocity magnitude of ~ 0.01 m/s inside the feed channel was observed, with a narrow region in the center, achieving a higher velocity magnitude in the range of ~ 0.06 to 0.07 m/s (Figs. 4A and B). Since there is no inlet velocity in the case of localized heating dead-end mode, the flow field evolution inside the feed channel was solely driven by the thermal convection which was generated by the heating coil. Consequently, the fluid movement was scattered, resulting in a significantly lower velocity magnitude (~ 0.001m/s) (Fig. 4C).

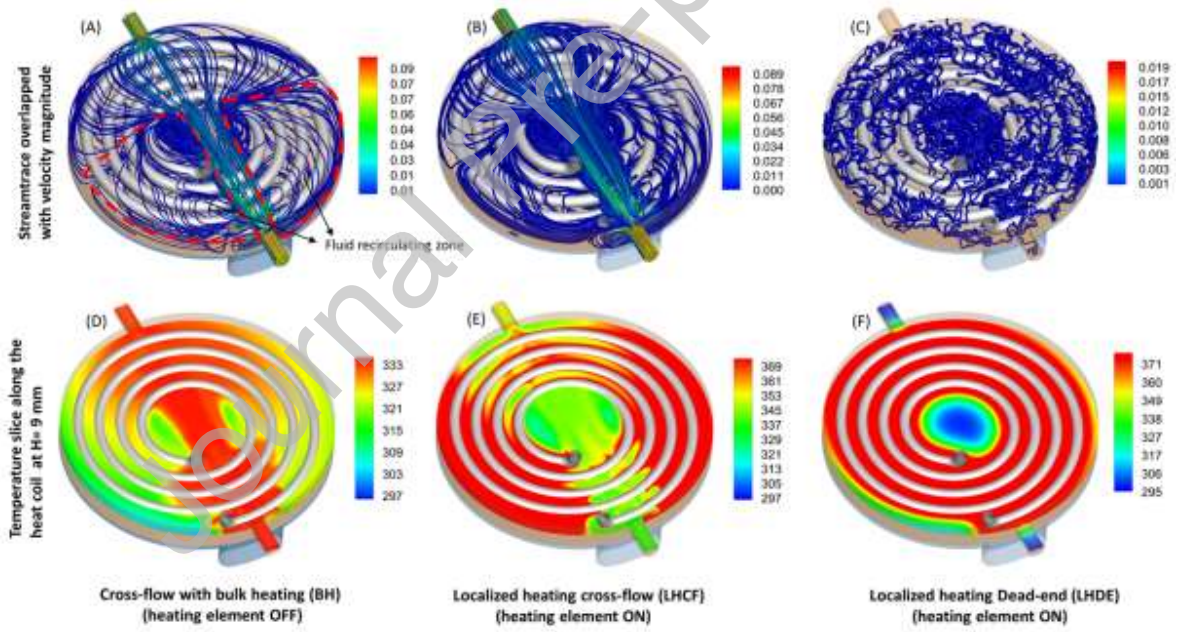

Fig. 4. Simulated flow hydrodynamic conditions using conjugate heat transfer model for different MD configurations: (A-C) stream trace overlapped with velocity magnitude, and (D-F) thermal snapshot slice along the heating coil at a depth H (9 mm) from the top of the feed channel.

The thermal snapshot is presented in the form of a spatial temperature distribution along a slice which was extracted from the top of a feed channel at a depth of 9 mm. This slice passed through the heating filament so that the associated thermal distribution and influence of localized heating could be visualized. In the case of a bulk heating mode, the feed liquid was heated outside the MD module. Consequently, the highest temperature was observed in the central region of the MD module (Fig. 4D) as the feed residence time in this region was shorter due to a higher fluid velocity (Fig. 4A), thereby allowing minimal heat dissipation. Contrarily, as indicated by lower feed temperatures (less than the feed inlet temperature), more heat dissipation was observed in the low velocity regions with existed fluid recirculation.

In the case of localized heating cross-flow, the spatial velocity and temperature distributions inside the module were completely reversed (Fig. 4E). As the incoming feed was not heated externally and the heating element was powered, the central region of the MD module had the lowest temperature (related to the design of the coil). Similar to the bulk heating mode, this effect was attributed to a higher feed flow velocity observed in this region, which did not allow enough residence time for the feed water to extract heat from the heating element. The low recirculating region, however, showed a significant increase in temperature with the maximum being in the range of 88 ^{o}C - 96 ^{o}C due to a larger heat transfer caused by increased fluid residence time. Furthermore, an asymmetry in temperature distribution was observed in the left and right recirculating regions. As seen in Fig. 4E, the left region was characterized by a slightly higher temperature as it had a larger recirculating region (Fig. 4A), thereby providing additional residence time for the fluid to extract the heat from the heating coil. Also, the ends of the heating coil were closer to this region, which also aided in supplying a larger coil surface area to improve the heat transfer. Finally, for the localized heating dead-

end case, an effective uniform feed heating was achieved due to a no-flow condition, as observed in Fig. 4F. The feed in the vicinity of the heating coil was effectively heated and the void region of the coil (central region) had the lowest temperature.

The heat distribution inside the feed channel was primarily governed by the interaction between the heating coil and the incoming feed through the convection process. However, at the membrane surface, the evaporation and heat loss by conduction primarily resulted in TP, which significantly altered surface temperatures on the feed and permeate sides of the membrane. As known, permeate flux which passes through the membrane pores, is solely dependent on the vapor pressure difference across the membrane (Khayet and Matsuura, 2011). Therefore, the membrane surface temperature is crucial and ultimately determines the performance of any MD configuration. To account for this effect, the spatial membrane surface temperatures were extracted and utilized to compute the vapor pressures using the Antoine equation (Eq. (10)). Permeate flux at each computational node on the surface was computed using the Knudsen-molecular diffusion, as described in Section 2.6.

Figs. 5 A-C show the membrane surface temperatures at the feed and permeate sides, as well as the spatial fluxes obtained through the numerical model for the MD configurations modelled in this work. For the case of bulk heating, the central membrane region had the highest temperature of ~ 60 ^{o}C, whereas the majority of other regions were characterized by lower temperatures in the range of ~ 33 ^{o}C - 45 ^{o}C. The heat losses by conduction and evaporation were visible in the central region on the permeate side, where permeate temperature increased locally. However, the highest permeate flux was still observed in the central region, which is attributed to the largest temperature gradient (corresponding to the highest vapor pressure difference) across the membrane surface. Similarly, in a localized

heating cross-flow configuration (powered heating element instead of fluid bulk heating), lower temperatures on the feed side were observed in the central region on both feed and permeate sides (Fig. 5B). Moreover, the high permeate flux region interchanged,–and higher local flux values were observed over a larger membrane surface area compared to that of a bulk heating configuration. The elevated permeate fluxes observed in the localized heating dead-end configuration were attributed to more uniform heat transfer from the heating coil, which resulted in increased feed water temperature (and corresponding temperature gradient) over a larger membrane surface area compared to the bulk heating configuration (Fig. 5C). As a result, the temperature gradients across the membrane and corresponding permeate fluxes were enhanced. Besides, TPC values shown in Fig. 5 indicate that highest polarization was observed in the BH mode (0.385), followed by the LHCF (0.437) and LHDE (0.514) modes. As a result, LHDE configuration was capable of effectively reducing TP by 33% as compared to that of BH mode. The spatial average values of permeate fluxes over the membrane surface were further calculated and compared to those obtained during actual MD experiments. As seen in Fig. 5D, the spatial average permeate fluxes predicted by the model had values of 4.86 $kg/m^{2}.h$, 8.43 $kg/m^{2}.h$ and 11.56 $kg/m^{2}.h$ for the bulk heating, localized heating cross-flow and localized heating dead-end, respectively, which is correlates well with permeate fluxes achieved experimentally when the feed temperature reached its pre-set value of 60 ^{o}C. The slight variation between the experimental and model results was attributed to the following factors: first, the heat loss to the ambient environment through the acrylic MD module could not be controlled, whereas, to simplify the simulations in adiabatic conditions, no heat loss from the outer boundary was assumed. Furthermore, possible membrane curvature inside the flow cell

may have affected some heat transfer and channel hydrodynamic characteristics, which are ignored in the present simulations.

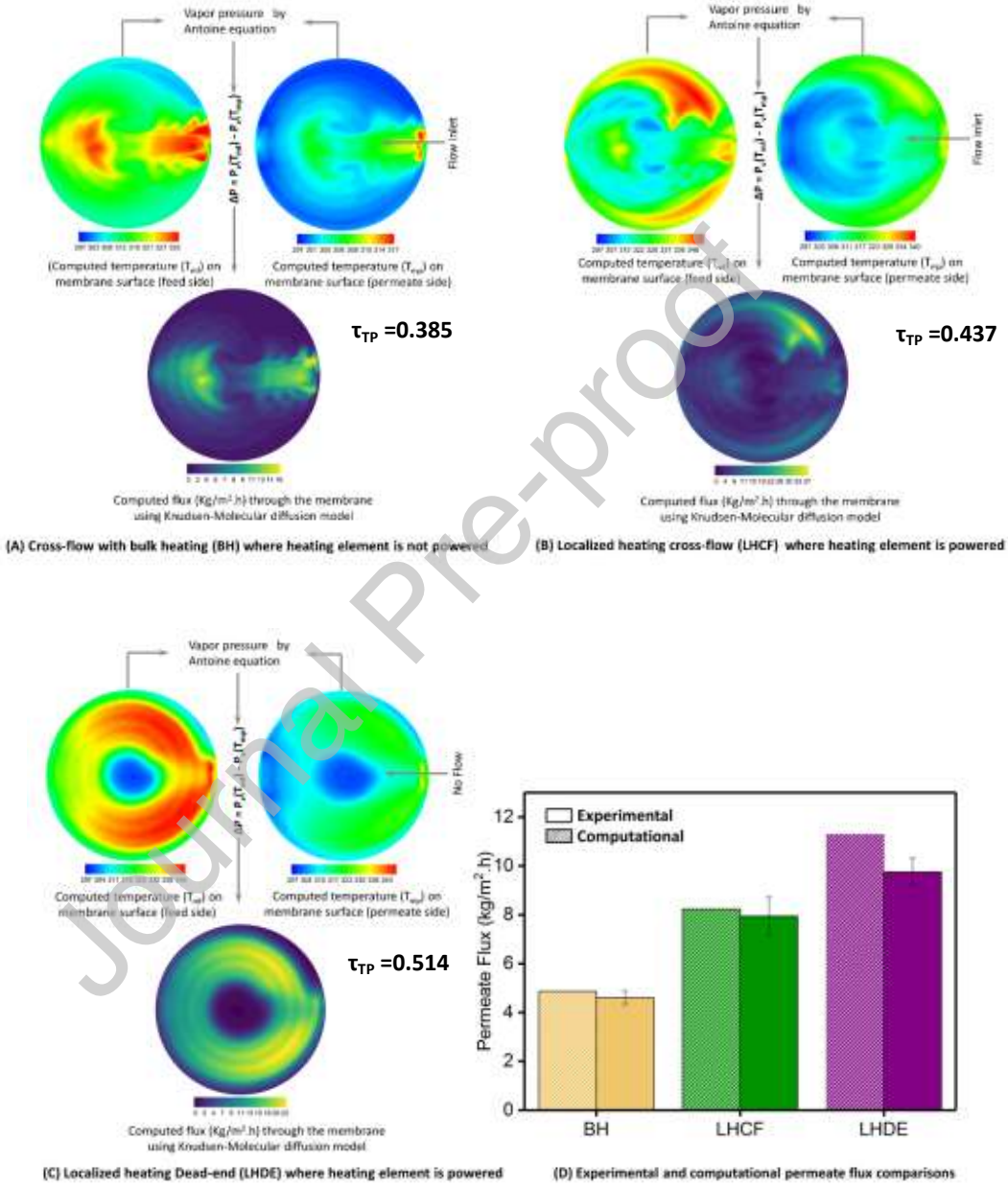

Fig. 5. (A-C) Computed membrane surface temperatures on feed and permeate sides along with spatial computed permeate fluxes for each MD configuration, and (D) comparison of highest experimental and

numerically simulated permeate flux values for different MD configurations. Corresponding TP coefficients (τ_{TP}) are also indicated for each configuration.

3.3. Energy analysis

Since MD is a thermally driven process, it requires a liquid-vapor phase change energy, called enthalpy of vaporization, which is two to three orders of magnitude higher than the Gibbs energy of separation required in the RO process, 650 kWh/m^3 versus 0.76 kWh/m^3 (0% recovery) in RO (Elimelech and Phillip, 2011; Semiat, 2008). Furthermore, the reported SEC and GOR values of the MD system are, albeit dispersed, reported in the range of 1 kWh/m^3 - 9,000 kWh/m^3 (Ghaffour et al., 2015; Khayet, 2013; Yang et al., 2014) and 0.1 - 5 (Summers et al., 2012), respectively. Herein, we comprehensively evaluated energy performance and heat transfer of the localized heating MD system and compared the results with those achieved in bulk heating MD to evaluate how the localized heating affects the MD specific energy consumption.

The total heat energy content of the feed flow are consumed through three main processes: circulation, conduction and evaporation. The circulation heat existed only in the case of bulk heating, calculated to be around 36 ± 4% of the total heat input. The circulation heat treated as wasted heat does not contribute to the distillation process. Unlike bulk heating, the localized heating mode has an incorporated electric heating coil and no circulation heat loss.

Since the localized heating cross-flow maintained a stable temperature across the membrane, the thermal boundary layer existed in its minimum form with the least TP. The total heat energy utilized in evaporation Q_{ev} and conduction Q_{cd} across the membrane was calculated using Eqs. (2) and (3), as shown in Fig. 6A. The Q_{cd} dominates over Q_{ev} in bulk

heating, at 50% and 29.6% respectively. It indicates the least amount of energy utilized in the distillation process. In localized heating cross-flow, the evaporation heat increased to 47.7% compared to the 29.6% in bulk heating. This illustrates the decrease in TP due to the inbuilt heating, which provides a stable temperature regime. Further, in localized heating cross-flow and localized heating dead-end with intermittent flush, the conduction heat loss decreased to around 33.6%, mainly due to the absence of feed circulation. However, the evaporation heat energy in the case of localized heating dead-end decreased from the localized heating cross-flow, mainly due to the effect of concentration accumulation after a certain time. A lower value of the heat required for evaporation could be attributed to the increased fouling accumulation at the membrane surface, which suppressed vapor evaporation at the pore entrance (Chen et al., 2020; Fortunato et al., 2018).

SEC values for all four MD configurations were calculated according to Eq. (4) and are shown in Fig. 6C. The bulk heating has the highest SEC value, around 2,762 kWh/m^3 ± 22 kWh/m^3. The localized heating cross-flow showed around a 44% decrease in SEC compared with the bulk heating. In localized heating dead-end and localized heating dead-end with intermittent flushing configurations, the SEC further decreased and reached the lowest value of 1183 kWh/m^3 for localized heating dead-end with intermittent flush. This significant decrease in SEC is attributed to the increase in the permeate production resulting from the localized heating. This elevated permeate water flux was caused by a decrease in TP and increased evaporation during the localized heating. Also, a rapid increase of the feed water temperature to its set value of 60 ^oC enhanced initial permeate flux and total permeate production so that the SEC values were reduced to 1,213 ± 139 kWh/m^3 and 1,183 ± 57 kWh/m^3 in localized heating dead-end and localized heating dead-end with intermittent flush, respectively. When comparing

calculated SEC values with the theoretical thermodynamic minimum energy of thermal evaporation, required to evaporate 1 kg of water (650 kWh/m^3 (Semiat, 2008), shown as a dashed line in Fig. 6C), we observed that the localized heating dead-end and localized heating dead-end with intermittent flush configurations were positioned almost twice as close to the thermodynamic minimum energy of evaporation value compared to that of the bulk heating mode. Moreover, the localized dead-end MD energy consumptions (4258 kJ/kg) demonstrated in this study are significantly lower than those reported previously for the conventional MD systems (118,000 kJ/kg for the DCMD (Luo and Lior, 2017) 42,696 kJ/kg for the vacuum MD (Song et al., 2019) and 82,800 kJ/kg for the air-gap MD (Alkhudhiri and Hilal, 2017)). Therefore, a 44% - 57% increase in specific energy efficiency improvements was achieved in localized heating modes (cross-flow and dead-end) due to reduced TP and enhanced water evaporation on the membrane surface, as shown in Fig. 6C.

The GOR values of bulk heating and localized heating were calculated as per Eq. (5) and shown in Fig. 6B. Bulk heating has the lowest GOR of ~ 0.24, increasing with the localized heating, which showed a 78% increase in localized heating cross-flow. The localized heating dead-end with intermittent flush showed the highest GOR value, ~ 0.6. The significant increase in the GOR value in localized heating is associated with the higher flux resulting from a decreased thermal boundary layer. Furthermore, the absence of a feed-flow condition inside the MD module and corresponding increase in evaporation allowed for a significant enhancement of GOR values during the dead-end localized heating (124 ± 21% and 132 ± 12% increases for the localized heating dead-end and localized heating dead-end with intermittent flush modes, respectively).

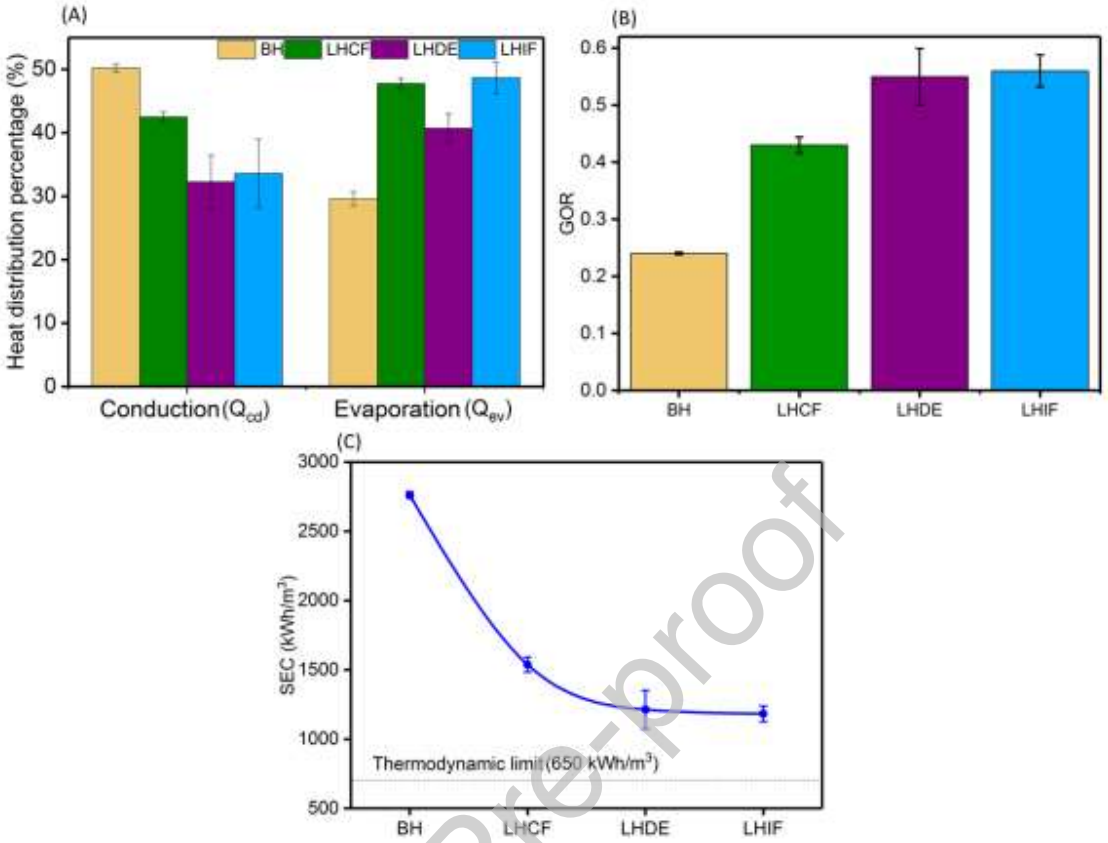

Fig. 6. (A) Percentage of heat distribution in the feed channel, the heat of evaporation and heat of conduction in various MD modes, (B) GOR of various MD configurations experiments, (C) SEC for different modes of localized heating. BH: conventional bulk heating, LHCF: localized heating cross-flow, LHDE: localized heating dead-end, and LHIF: localized heating dead-end with intermittent flush.

3.4. Effect of the localized heating on membrane integrity and morphology

Given that the heating coil inside the MD module is located next to the membrane surface, it is essential to determine if localized heating would impose any adverse effects on the surface of the polymeric membrane. The changes in the membrane's integrity and morphology were evaluated by a range of surface characterization techniques, including SEM, ATR FT-IR and contact angle measurements. A comparison of SEM images of a virgin membrane with the membrane subjected to localized heating (Figs. 7A and B) revealed no changes in surface

morphology after surface heating, so that both images exhibited typical node-like PTFE structures. This observation was further supported by the results of the ATR FT-IR spectroscopy (Fig. 7C) with both membrane surfaces producing characteristic PTFE bands at 1204 cm^{-1}, 1150 cm^{-1} and 637 cm^{-1}. These bands were ascribed to the asymmetrical stretching, symmetrical stretching and waggling of CF_2 groups, respectively (Piwowarczyk et al., 2019). The contact angle measurements revealed no significant difference between the virgin and after surface heating surfaces ($135.1^o \pm 2.8$ and $131.2^o \pm 1.1$, respectively) (Figs. 7D and E). Hence, it can be concluded that localized heating did not compromise membrane integrity nor affect its morphological properties. Yet, we suggest the use of custom-made flexible coils specifically designed for this application to be used for different module geometries aiming to eliminate dead zones (Ali et al., 2019; Qamar et al., 2019).

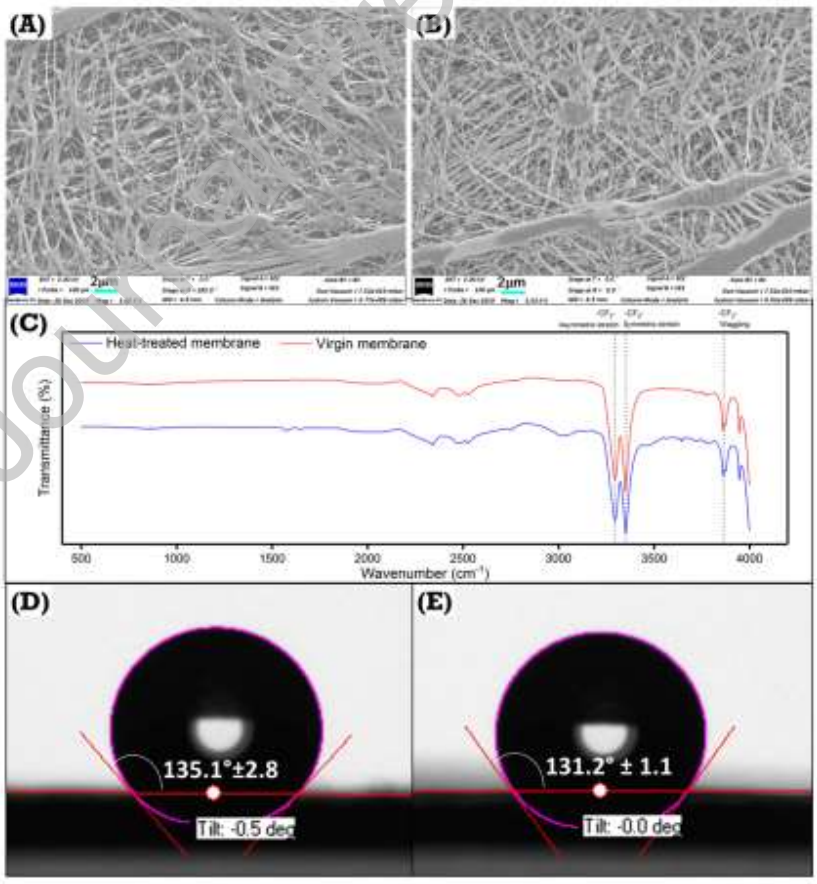

Fig. 7. (A-B) SEM images of the virgin membrane surface and membrane surface after localized heating, respectively, (C) ATR FT-IR spectra of virgin and heat-treated membrane, (D, E) contact angles of the virgin membrane surface and localized heated membrane surface, respectively.

4. Future prospects

This proposed work aims to minimize the problem of intrinsic MD process deficiency. The phenomenon of TP which stems from the heat losses during water evaporation and conduction loss imposes substantial process limitations. As a result, MD performance and permeate production are impended. The localized heating targets fundamental issue of TP and offers innovative approach to mitigate this phenomenon so that thermal efficiency and permeate production are improved. Significant difference of this technology from the existing ones is that localized heating is capable of delivering thermal energy directly to the feed water/membrane interface throughout the entire feed channel length by utilizing Joule heating elements so that the stable feed temperature is maintained.

In terms of process control and scalability, several routs are proposed. For instance, Joule heating inside the MD module can be achieved by filling the feed channel with metallic spacers (Tan et al., 2020). Similarly, to incorporate localized heating into a spiral wound module, thin Nichrome wire mesh or Nichrome wire weaved in polymeric spacer can be employed. In case of a hollow-fiber module, a hollow-fiber bundle can be inserted between the two helical-shaped heating elements to ensure that both inner and outer fibers are equally heated. Alternatively, a thin heating element could be pulled through the fiber lumen to provide precise heating of each fiber. Although these approaches deem viable, they require sophisticated and accurate temperature control system to ensure process integrity. Application of multiple thermistors

with the feedback controlled by the artificial intelligence technologies would be a potential future direction to transfer the localized heating technology to a commercial scale.

5. Conclusions

In this study, we have successfully applied localized heating by incorporating an electric heating coil inside the MD module. Different configurations, including a new dead-end MD mode, were investigated numerically and validated through a series of experiments. Results showed that dead-end MD with localized heating outperformed all the other configurations in terms of vapor flux and energy consumption, mainly due to the minimization of TP caused by temperature stratification occurring in conventional MD. The introduction of intermittent flush to the dead-end concept further improved the MD performance by reducing membrane fouling and associated heat losses. Modeling results revealed that localized heating provided more uniform heat transfer across the membrane due to increased feed water temperature over a larger membrane area. As a result, the TP across the membrane was mitigated and corresponding permeate fluxes were enhanced. Dead-end localized heating showed:

- 10% - 45% increase in water vapor flux for the different configurations
- 44% - 57% decrease in specific energy consumption for cross-flow and dead-end modes reaching 1183 kWh/m^3 (dead-end), thus approaching the thermodynamic minimum energy limit for water evaporation (650 kWh/m^3)
- increase of GOR values by 132 ± 12%.

The surface characterization techniques confirmed no changes in membrane integrity and morphology after prolonged surface heating, which provides a promising new framework for sustainable MD development. Therefore, we expect that the combined effect of localized

heating and intermittent flush in dead-end mode will enable more sustainable MD for long-term operations by maintaining more stable vapor flux while alleviating membrane fouling and minimizing energy consumption.

Author contribution

M.M, A.Q. and N.G. conceived the project and designed the experiments. M.M. fabricated the module and performed the experiments. A.Q. wrote the code and performed simulations. A.A. did the characterization, methodology and data analysis. N.G. supervised the project. All authors discussed the results, gave comments and edited the manuscript.

Conflict of interest

The authors declare no competing interests.

Acknowledgements

The research reported in this paper was supported by King Abdullah University of Science and Technology (KAUST), Saudi Arabia. The authors acknowledge help, assistance and support from the Water Desalination and Reuse Center (WDRC) and KAUST Supercomputing Laboratory (KSL) staff.

Graphical abstract

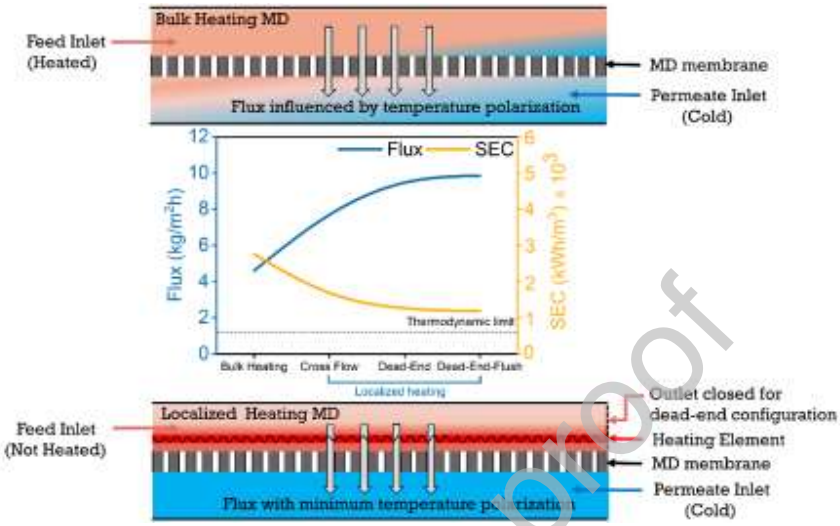

Reference

Ali, S.M., Qamar, A., Kerdi, S., Phuntsho, S., Vrouwenvelder, J.S., Ghaffour, N. and Shon, H.K. 2019. Energy efficient 3D printed column type feed spacer for membrane filtration. Water Research 164, 114961.

Alkhudhiri, A. and Hilal, N. 2017. Air gap membrane distillation: A detailed study of high saline solution. Desalination 403, 179-186.

Alsaadi, A.S., Alpatova, A., Lee, J.-G., Francis, L. and Ghaffour, N. 2018. Flashed-feed VMD configuration as a novel method for eliminating temperature polarization effect and enhancing water vapor flux. Journal of Membrane Science 563, 175-182.

Alsaadi, A.S., Francis, L., Maab, H., Amy, G.L. and Ghaffour, N. 2015. Evaluation of air gap membrane distillation process running under sub-atmospheric conditions: Experimental and simulation studies. Journal of Membrane Science 489, 73-80.

Andrés-Mañas, J.A., Ruiz-Aguirre, A., Acién, F.G. and Zaragoza, G. 2018. Assessment of a pilot system for seawater desalination based on vacuum multi-effect membrane distillation with enhanced heat recovery. Desalination 443, 110-121.

ANSYS 2019 Release 19.0, ANSYS Fluent Theory Guide, ANSYS Inc.

Anvari, A., Kekre, K.M., Azimi Yancheshme, A., Yao, Y. and Ronen, A. 2019. Membrane distillation of high salinity water by induction heated thermally conducting membranes. Journal of Membrane Science 589.

Boo, C. and Elimelech, M. 2017. Thermal desalination membranes: Carbon nanotubes keep up the heat. Nature nanotechnology 12(6), 501-503.

Caldera, U. and Breyer, C. 2017. Learning Curve for Seawater Reverse Osmosis Desalination Plants: Capital Cost Trend of the Past, Present, and Future. Water Resources Research 53(12), 10523-10538.

Chen, X., Vanangamudi, A., Wang, J., Jegatheesan, J., Mishra, V., Sharma, R., Gray, S.R., Kujawa, J., Kujawski, W., Wicaksana, F. and Dumée, L.F. 2020. Direct contact membrane distillation for effective concentration of perfluoroalkyl substances – Impact of surface fouling and material stability. Water research 182, 116010.

Curcio, E. and Drioli, E. 2005. Membrane Distillation and Related Operations—A Review. Separation & Purification Reviews 34(1), 35-86.

Dongare, P.D., Alabastri, A., Pedersen, S., Zodrow, K.R., Hogan, N.J., Neumann, O., Wu, J., Wang, T., Deshmukh, A., Elimelech, M., Li, Q., Nordlander, P. and Halas, N.J. 2017. Nanophotonics-enabled solar membrane distillation for off-grid water purification. Proc Natl Acad Sci U S A 114(27), 6936-6941.

Dudchenko, A.V., Chen, C., Cardenas, A., Rolf, J. and Jassby, D. 2017. Frequency-dependent stability of CNT Joule heaters in ionizable media and desalination processes. Nature nanotechnology 12(6), 557-563.

Elcik, H., Fortunato, L., Alpatova, A., Soukane, S., Orfi, J., Ali, E., AlAnsary, H., Leiknes, T. and Ghaffour, N. 2020. Multi-effect distillation brine treatment by membrane distillation: Effect of antiscalant and antifoaming agents on membrane performance and scaling control. Desalination 493.

Eleiwi, F., Ghaffour, N., Alsaadi, A.S., Francis, L. and Laleg-Kirati, T.M. 2016. Dynamic modeling and experimental validation for direct contact membrane distillation (DCMD) process. Desalination 384, 1-11.

Elimelech, M. and Phillip, W.A. 2011. The future of sea water desalination. Science 333.

Elmarghany, M.R., El-Shazly, A.H., Salem, M.S., Sabry, M.N. and Nady, N. 2019. Thermal analysis evaluation of direct contact membrane distillation system. Case Studies in Thermal Engineering 13, 100377.

Fane, A.G., Schofield, R.W. and Fell, C.J.D. 1987. The efficient use of energy in membrane distillation. Desalination 64, 231-243.

Fortunato, L., Jang, Y., Lee, J.G., Jeong, S., Lee, S., Leiknes, T. and Ghaffour, N. 2018. Fouling development in direct contact membrane distillation: Non-invasive monitoring and destructive analysis. Water research 132, 34-41.

Ghaffour, N., Bundschuh, J., Mahmoudi, H. and Goosen, M.F.A. 2015. Renewable energy-driven desalination technologies: A comprehensive review on challenges and potential applications of integrated systems. Desalination 356, 94-114.

Ghaffour, N., Missimer, T.M. and Amy, G.L. 2013. Combined desalination, water reuse, and aquifer storage and recovery to meet water supply demands in the GCC/MENA region. Desalination and Water Treatment 51(1-3), 38-43.

IDA 2015 International Desalination Association Desalination Yearbook 2015-2016 Rollinson, O. and Owen, R. (eds), Global Water Intelligence (GWI).

Jantaporn, W., Ali, A. and Aimar, P. 2017. Specific energy requirement of direct contact membrane distillation. Chemical Engineering Research and Design 128, 15-26.

Jiang, L., Chen, L. and Zhu, L. 2019. Electrically conductive membranes for anti-biofouling in membrane distillation with two novel operation modes: Capacitor mode and resistor mode. Water research 161, 297-307.

Jones, E., Qadir, M., van Vliet, M.T.H., Smakhtin, V. and Kang, S.M. 2019. The state of desalination and brine production: A global outlook. Sci Total Environ 657, 1343-1356.

Khayet, M. 2013. Solar desalination by membrane distillation: Dispersion in energy consumption analysis and water production costs (a review). Desalination 308, 89-101.

Khayet, M. and Matsuura, T. (2011) Membrane Distillation. Khayet, M. and Matsuura, T. (eds), pp. 249-293, Elsevier, Amsterdam.

Kim, Y.-D., Francis, L., Lee, J.-G., Ham, M.-G. and Ghaffour, N. 2018. Effect of non-woven net spacer on a direct contact membrane distillation performance: Experimental and theoretical studies. Journal of Membrane Science 564, 193-203.

Kim, Y.D., Thu, K., Ng, K.C., Amy, G.L. and Ghaffour, N. 2016. A novel integrated thermal-/membrane-based solar energy-driven hybrid desalination system: Concept description and simulation results. Water research 100, 7-19.

Koschikowski, J. 2003. Solar thermal-driven desalination plants based on membrane distillation

L Martinez, D. and Diaz, F. 1998. Study of membrane distillation using channel spacers. Journal of Membrane Science 144.

Lee, J.G., Kim, W.S., Choi, J.S., Ghaffour, N. and Kim, Y.D. 2016. A novel multi-stage direct contact membrane distillation module: Design, experimental and theoretical approaches. Water research 107, 47-56.

Lokare, O.R., Tavakkoli, S., Khanna, V. and Vidic, R.D. 2018. Importance of feed recirculation for the overall energy consumption in membrane distillation systems. Desalination 428, 250-254.

Luo, A. and Lior, N. 2017. Study of advancement to higher temperature membrane distillation. Desalination 419, 88-100.

Naji, O., Al-Juboori, R.A., Bowtell, L., Alpatova, A. and Ghaffour, N. 2020. Direct contact ultrasound for fouling control and flux enhancement in air-gap membrane distillation. Ultrason Sonochem 61, 104816.

Olatunji, S.O. and Camacho, L.M. 2018. Heat and Mass Transport in Modeling Membrane Distillation Configurations: A Review. Frontiers in Energy Research 6.

Piwowarczyk, J., Jedrzejewski, R., Moszynski, D., Kwiatkowski, K., Niemczyk, A. and Baranowska, J. 2019. XPS and FTIR Studies of Polytetrafluoroethylene Thin Films Obtained by Physical Methods. Polymers (Basel) 11(10).

Plattner, J., Naidu, G., Wintgens, T., Vigneswaran, S. and Kazner, C. 2017. Fluoride removal from groundwater using direct contact membrane distillation (DCMD) and vacuum enhanced DCMD (VEDCMD). Separation and Purification Technology 180, 125-132.

Politano, A., Argurio, P., Di Profio, G., Sanna, V., Cupolillo, A., Chakraborty, S., Arafat, H.A. and Curcio, E. 2017. Photothermal Membrane Distillation for Seawater Desalination. Advanced materials 29(2).

Qamar, A., Bucs, S., Picioreanu, C., Vrouwenvelder, J. and Ghaffour, N. 2019. Hydrodynamic flow transition dynamics in a spacer filled filtration channel using direct numerical simulation. Journal of Membrane Science 590, 117264.

Qamar, A., Hasan, N. and Sanghi, S. 2014. A New Spatial Discretization Strategy of the Convective Flux Term for the Hyperbolic Conservation Laws. Engineering Applications of Computational Fluid Mechanics 4(4), 593-611.

Qtaishat, M.R. and Banat, F. 2013. Desalination by solar powered membrane distillation systems. Desalination 308, 186-197.

Rezaei, M., Warsinger, D.M., Lienhard, V.J., Duke, M.C., Matsuura, T. and Samhaber, W.M. 2018. Wetting phenomena in membrane distillation: Mechanisms, reversal, and prevention. Water research 139, 329-352.

Rogers, G. and Y, M. (2009) Steam table: Thermodynamic and Transport Properties of Fluids, Blackwell.

Sanmartino, J.A., Khayet, M., García-Payo, M.C., El-Bakouri, H. and Riaza, A. 2017. Treatment of reverse osmosis brine by direct contact membrane distillation: Chemical pretreatment approach. Desalination 420, 79-90.

Santoro, S., Vidorreta, I.M., Sebastian, V., Moro, A., Coelhoso, I.M., Portugal, C.A.M., Lima, J.C., Desiderio, G., Lombardo, G., Drioli, E., Mallada, R., Crespo, J.G., Criscuoli, A. and Figoli, A. 2017. A non-invasive optical method for mapping temperature polarization in direct contact membrane distillation. Journal of Membrane Science 536, 156-166.

Schwantes, R., Bauer, L., Chavan, K., Dücker, D., Felsmann, C. and Pfafferott, J. 2018. Air gap membrane distillation for hypersaline brine concentration: Operational analysis of a full-scale module–New strategies for wetting mitigation. Desalination 444, 13-25.

Semiat, R. 2008. Energy Issues in Desalination Processes. American Chemical Society 42(22).

Seo, J., Kim, Y.M. and Kim, J.H. 2017. Spacer optimization strategy for direct contact membrane distillation: Shapes, configurations, diameters, and numbers of spacer filaments. Desalination 417, 9-18.

Shakaib, M., Hasani, S.M.F., Ahmed, I. and Yunus, R.M. 2012. A CFD study on the effect of spacer orientation on temperature polarization in membrane distillation modules. Desalination 284, 332-340.

Shim, W.G., He, K., Gray, S. and Moon, I.S. 2015. Solar energy assisted direct contact membrane distillation (DCMD) process for seawater desalination. Separation and Purification Technology 143, 94-104.

Shukla, S., Benes, N.E., Vankelecom, I., Méricq, J.P., Belleville, M.P., Hengl, N. and Marcano, J.S. 2015. Sweep gas membrane distillation in a membrane contactor with metallic hollow-fibers. Journal of Membrane Science 493, 167-178.

Song, L., Huang, Q., Huang, Y., Bi, R. and Xiao, C. 2019. An electro-thermal braid-reinforced PVDF hollow fiber membrane for vacuum membrane distillation. Journal of Membrane Science 591.

Soukane, S., Naceur, M.W., Francis, L., Alsaadi, A. and Ghaffour, N. 2017. Effect of feed flow pattern on the distribution of permeate fluxes in desalination by direct contact membrane distillation. Desalination 418, 43-59.

Subramani, A. and Jacangelo, J.G. 2015. Emerging desalination technologies for water treatment: a critical review. Water research 75, 164-187.

Subramanian, N., Qamar, A., Alsaadi, A., Gallo Jr, A., Ridwan, M.G., Lee, J.-G., Pillai, S., Arunachalam, S., Anjum, D. and Sharipov, F. 2019. Evaluating the potential of superhydrophobic nanoporous alumina membranes for direct contact membrane distillation. Journal of Colloid and Interface Science 533, 723-732.

Summers, E.K., Arafat, H.A. and Lienhard, J.H. 2012. Energy efficiency comparison of single-stage membrane distillation (MD) desalination cycles in different configurations. Desalination 290, 54-66.

Taamneh, Y. and Bataineh, K. 2017. Improving the performance of direct contact membrane distillation utilizing spacer-filled channel. Desalination 408, 25-35.

Tan, Y.Z., Chandrakant, S.P., Ang, J.S.T., Wang, H. and Chew, J.W. 2020. Localized induction heating of metallic spacers for energy-efficient membrane distillation. Journal of Membrane Science 606.

Tan, Y.Z., Wang, H., Han, L., Tanis-Kanbur, M.B., Pranav, M.V. and Chew, J.W. 2018. Photothermal-enhanced and fouling-resistant membrane for solar-assisted membrane distillation. Journal of Membrane Science 565, 254-265.

Wang, H. 2018. Low-energy desalination. Nature nanotechnology 13(4), 273-274.

Wang, P. and Chung, T.-S. 2015. Recent advances in membrane distillation processes: Membrane development, configuration design and application exploring. Journal of Membrane Science 474, 39-56.

Wu, X., Jiang, Q., Ghim, D., Singamaneni, S. and Jun, Y.-S. 2018. Localized heating with a photothermal polydopamine coating facilitates a novel membrane distillation process. Journal of Materials Chemistry A 6(39), 18799-18807.

Yang, X., Fane, A.G. and Wang, R. (2014) Desalination, pp. 373-424, John Wiley & Sons, Inc.

Ye, H., Li, X., Deng, L., Li, P., Zhang, T., Wang, X. and Hsiao, B.S. 2019. Silver Nanoparticle-Enabled Photothermal Nanofibrous Membrane for Light-Driven Membrane Distillation. Industrial & Engineering Chemistry Research 58(8), 3269-3281.